The Astrophysical Journal, 710:1335–1342, 2010 February 20 doi:10.1088/0004-637X/710/2/1335

MAGNETAR TWISTS: *FERMI*/GAMMA-RAY BURST MONITOR DETECTION OF SGR J1550–5418

Yuki Kaneko[1], Ersin Göğüş[1], Chryssa Kouveliotou[2], Jonathan Granot[3], Enrico Ramirez-Ruiz[4], Alexander J. van der Horst[2], Anna L. Watts[5], Mark H. Finger[6], Neil Gehrels[7], Asaf Pe'er[8], Michiels van der Klis[5], Andreas von Kienlin[9], Stefanie Wachter[10], Colleen A. Wilson-Hodge[2], and Peter M. Woods[11]
[1] SabancıUniversity, Orhanlı-Tuzla, İstanbul 34956, Turkey; yuki@sabanciuniv.edu
[2] Space Science Office, VP62, NASA/Marshall Space Flight Center, Huntsville, AL 35812, USA
[3] Centre for Astrophysics Research, University of Hertfordshire, College Lane, Hatfield AL10 9AB, UK
[4] Department of Astronomy and Astrophysics, University of California, Santa Cruz, CA 95064, USA
[5] Astronomical Institute ÒAnton Pannekoek,Ó University of Amsterdam, P.O. Box 94249, 1090 GE Amsterdam, The Netherlands
[6] Universities Space Research Associations, NSSTC, Huntsville, AL 35805, USA
[7] NASA/Goddard Space Flight Center, Greenbelt, MD 20771, USA
[8] Space Telescope Science Institute, 3700 San Martin Dr., Baltimore, MD 21218, USA
[9] Max-Planck Institut für extraterrestrische Physik, 85748 Garching, Germany
[10] Spitzer Science Center/California Institute of Technology, Pasadena, CA 91125, USA
[11] Dynetics, Inc., 1000 Explorer Boulevard, Huntsville, AL 35806, USA
Received 2009 December 11; accepted 2009 December 22; published 2010 January 29

ABSTRACT

SGR J1550–5418 (previously known as AXP 1E 1547.0–5408 or PSR J1550–5418) went into three active bursting episodes in 2008 October and in 2009 January and March, emitting hundreds of typical soft gamma repeater bursts in soft gamma rays. The second episode was especially intense, and our untriggered burst search on *Fermi*/Gamma-ray Burst Monitor (GBM) data (8–1000 keV) revealed ∼450 bursts emitted over 24 hr during the peak of this activity. Using the GBM data, we identified a ∼150 s long enhanced persistent emission during 2009 January 22 that exhibited intriguing timing and spectral properties: (1) clear pulsations up to ∼110 keV at the spin period of the neutron star ($P \sim 2.07$ s, the fastest of all magnetars); (2) an additional (to a power-law) blackbody component required for the enhanced emission spectra with $kT \sim 17$ keV; and (3) pulsed fraction that is strongly energy dependent and highest in the 50–74 keV energy band. A total isotropic-equivalent energy emitted during this enhanced emission is estimated to be $2.9 \times 10^{40}(D/5\ \mathrm{kpc})^2$ erg. The estimated area of the blackbody emitting region of $\approx 0.046(D/5\ \mathrm{kpc})^2$ km^2 (roughly a few $\times 10^{-5}$ of the neutron star area) is the smallest "hot spot" ever measured for a magnetar and most likely corresponds to the size of magnetically confined plasma near the neutron star surface.

Key words: pulsars: individual (SGR J1550−5418, 1E 1547.0−5408, PSR J1550–5418) – stars: neutron – X-rays: bursts

1. INTRODUCTION

A very small group (roughly half a dozen) of isolated neutron stars have manifested themselves in one class as soft gamma repeaters (SGRs) linked by numerous common distinguishing properties. Among the most characteristic SGR attributes are (1) X-ray luminosities much larger (by ∼100 times) than the ones expected from their rotational energy losses, and (2) the emission of repeated bursts of soft gamma rays. SGR bursts range from "typical" short events lasting ∼0.1 s with peak luminosities of $L_p \lesssim 10^{41}$ erg s^{-1}, to occasional intermediate flares lasting a few seconds with $L_p \sim 10^{42}$–10^{43} erg s^{-1}, and finally to—extremely rare—giant flares lasting a few hundred seconds with $L_p \gtrsim 10^{45}$ erg s^{-1}. SGRs were identified together with Anomalous X-ray Pulsars (AXPs) as "magnetars": neutron stars powered by their extremely strong magnetic fields (surface dipole $B \sim 10^{14-15}$ G; Duncan & Thompson 1992; Kouveliotou et al. 1998). Comprehensive reviews on magnetars can be found in Woods & Thompson (2006) and Mereghetti (2008), and references therein.

1E 1547.0–5408 was observed with the X-ray Multi-mirror Mission (*XMM-Newton*) in 2004 as a magnetar candidate, selected for its Galactic plane location and its relatively soft magnetar-like spectrum as seen with the *Advanced Satellite for Cosmology and Astrophysics* (*ASCA*) during their Galactic plane survey (Sugizaki et al. 2001). Although no period was detected in the original and follow-up *XMM* observations, Gelfand & Gaensler (2007) also proposed 1E 1547.0–5408 as a magnetar candidate based on its spectrum and its positional coincidence with an extended galactic radio source G327.24−0.13 (possibly a supernova remnant). The subsequent discovery in radio observations of a spin period of 2.07 s and a period derivative of 2.3×10^{-11} s s^{-1} led to an estimated dipole surface field of $B \sim 2.2 \times 10^{14}$ G and confirmed the source's magnetar nature; the source was also renamed as PSR J1550–5418 (Camilo et al. 2007). Its period makes 1E 1547.0–5408 the fastest rotating magnetar; the source is also one of the only two that emit in radio wavelengths (the other source is an AXP, *XTE* J1810−197; Halpern et al. 2005; Camilo et al. 2006). The distance of the source has been estimated by different authors using various methods: Camilo et al. (2007) found a distance of ≈9 kpc by measuring radio dispersion; Gelfand & Gaensler (2007) estimated ≈4 kpc assuming an association of the source with a possible supernova remnant, G327.24−0.13; and most recently Tiengo et al. (2010) reported an average distance of 4–5 kpc by using observations of an X-ray scattering halo in the *Swift*/X-ray Telescope (XRT) data. Throughout this paper, we use $D_5 = D/5$ kpc as the source distance measure.

On 2008 October 3, 1E 1547.0–5408 entered an episode of X-ray activity, emitting several typical SGR-like bursts over the next 7 days. During this period, 22 short duration bursts were observed with the Gamma-ray Burst Monitor (GBM) on board the *Fermi Gamma-ray Space Telescope*. A detailed analysis of these events is presented in A. von Kienlin et al. (2010, in preparation).

On 2009 January 22, the source entered a second period of extremely high X-ray burst activity (Mereghetti et al. 2009). During the first 24 hr of this "storm," the *Fermi*/GBM triggered

on the source 41 times: the number of triggers was limited only by the instrument's capability and did not reflect the actual number of bursts emitted by the source. In fact, our on-ground search for untriggered events revealed a total of ∼450 bursts during this 24 hr period: an unusually high burst frequency from a single source (A. J. van der Horst et al. 2010, in preparation). Based on this SGR-like behavior, we renamed the source as SGR J1550–5418 (Kouveliotou et al. 2009).

Upon examination of the data from the first GBM trigger on January 22, we identified 29 short events riding on an enhancement of the underlying persistent emission lasting ∼150 s. Closer inspection of this enhancement in different energy ranges revealed periodic oscillations with a period consistent with the spin period of SGR J1550–5418. We present here a detailed temporal and spectral analysis of this enhanced emission period. In Section 2, we briefly describe our observations and the GBM instrument and data types. We present our temporal analysis results in Section 3, and our spectral studies in Section 4. Finally, we discuss the physical implications of our discovery in Section 5.

2. INSTRUMENTATION AND DATA

The *Fermi*/GBM consists of 12 Na I detectors (8–1000 keV) arranged in four clusters of three each and two BGO detectors (0.20–40 MeV) at opposite sides of the spacecraft (for a detailed description of the instrument, see Meegan et al. 2009). GBM is currently the only instrument with continuous broadband energy coverage (8 keV–40 MeV) and a wide field of view (8 sr after taking into account occultation by the Earth) and is, therefore, uniquely positioned to accomplish a comprehensive magnetar (or any transient event) monitoring. In trigger mode, GBM provides three types of data; CTIME Burst, CSPEC Burst, and time-tagged event (TTE) data (Meegan et al. 2009). The CTIME Burst data have time resolution of 64 ms with rather coarse spectral information (eight energy channels). The CSPEC Burst data provide high-resolution spectra (128 energy channels) collected every 1.024 s. Both CTIME Burst and CSPEC Burst accumulate data for ∼600 s after a trigger. The TTE data provide time-tagged photon event lists for an accumulation time of 330 s, starting 30 s prior to the trigger time; this data type provides superior temporal resolution down to 2 μs at the same spectral resolution as the CSPEC Burst data.

The first GBM trigger at the onset of the second active episode from SGR J1550–5418 was on 2009 January 22 at 00:53:52.17 UT (= T_0, GBM trigger number 090122037). In the 600 s of the trigger readout, we detected many individual short bursts using our on-ground untriggered burst search algorithm. To accept an event as an untriggered burst, we required excess count rates of at least 5.5σ and 4.5σ in the first and second brightest detectors, respectively, in the 10–300 keV energy range. We used CTIME data in both continuous (256 ms time resolution) and Burst mode (64 ms resolution). Subsequently, we inspected energy-resolved burst morphology and compared each detector zenith angle to the source for all 12 detectors, to determine whether the events originated from SGR J1550–5418. In total, we identified about a dozen very bright bursts and over 40 less intense bursts within 600 s after T_0 (see Figure 1). During the same trigger readout, we also discovered an enhancement in the underlying persistent emission starting at approximately T_0 + 70 s and lasting for ∼150 s (see the inset of Figure 1).

One of the events recorded during these 600 s, specifically the burst at T_0+147 s, was so bright that it initiated an autonomous repoint recommendation (ARR), causing the spacecraft to start slewing toward the SGR J1550–5418 direction. As the source was already close to the boresight of the Large Area Telescope (LAT), the slew angle was pretty small. However, we proceeded to check whether the observed emission enhancement was artificially caused by the spacecraft slewing. First, we calculated the variation in time of the zenith angle of SGR J1550–5418 for each of the 12 GBM detectors. At the onset of the enhancement (T_0 + 70 s), the Na I 0 detector had the smallest zenith angle to the source of 15°. Due to the ARR, Na I 0 kept a constant angle of 18° to the source from T_0 + 150 s to T_0 + 210 s, after which it constantly slewed away from the source until it reached an angle of 23° at T_0 + 270 s. During this time the persistent emission kept rising until T_0 + 150 s, which alone confirms that the enhanced emission is intrinsic to SGR J1550–5418. The source was in the field of view of the detector until ∼T_0 + 225 s, at which time it went into an occultation by the LAT. At the same time, Na I 6 was slewing toward the source at an angle of 20°, but the emission was unfortunately obscured by the LAT until ∼T_0 + 225 s. We note, however, that the enhanced emission was not clearly detected with Na I 6 after T_0 + 225 s. Based on the above, we conclude that the rise of the enhanced emission was definitely not caused by the spacecraft slew but by the source itself; we cannot unambiguously determine the end of the decay trend (or the total duration of the enhancement) in the data due to LAT obscuration. In the analysis presented in this paper, we have exclusively used data from Na I 0 (unless noted otherwise), to avoid any obscuration effects. Finally, we also checked the LAT data (20 MeV–300 GeV) of the entire day for associated high-energy gamma-ray emission, but found no evidence of high-energy photons originating from the direction of SGR J1550–5418.

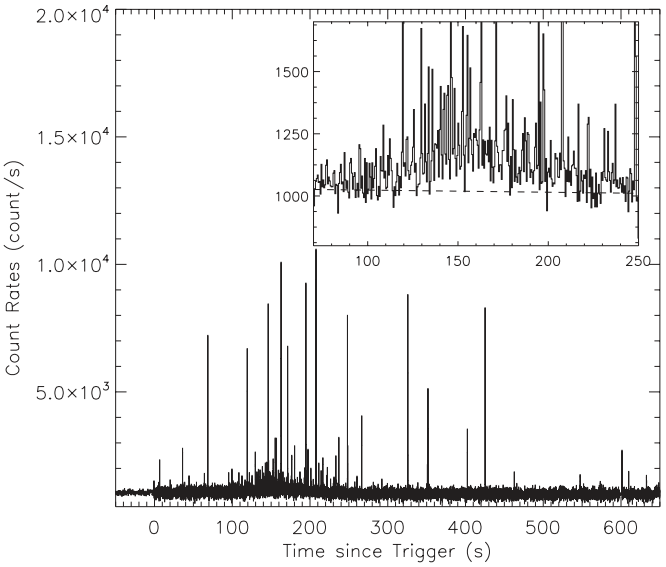

Figure 1. Light curve of SGR J1550–5418 in 12–293 keV (GBM Na I 0 CTIME data channels 1–4). An enlarged view of the pulsed, enhanced emission is shown in the inset. The dashed line indicates the background level.

3. TEMPORAL PROPERTIES OF PULSED HARD X-RAYS

3.1. Timing Analysis

During our search for untriggered events in the first trigger interval of 2009 January 22 from SGR J1550–5418, we found strong apparent periodic modulations in the enhanced emission period from T_0 + 130 to 160 s in the 50–102 keV data of

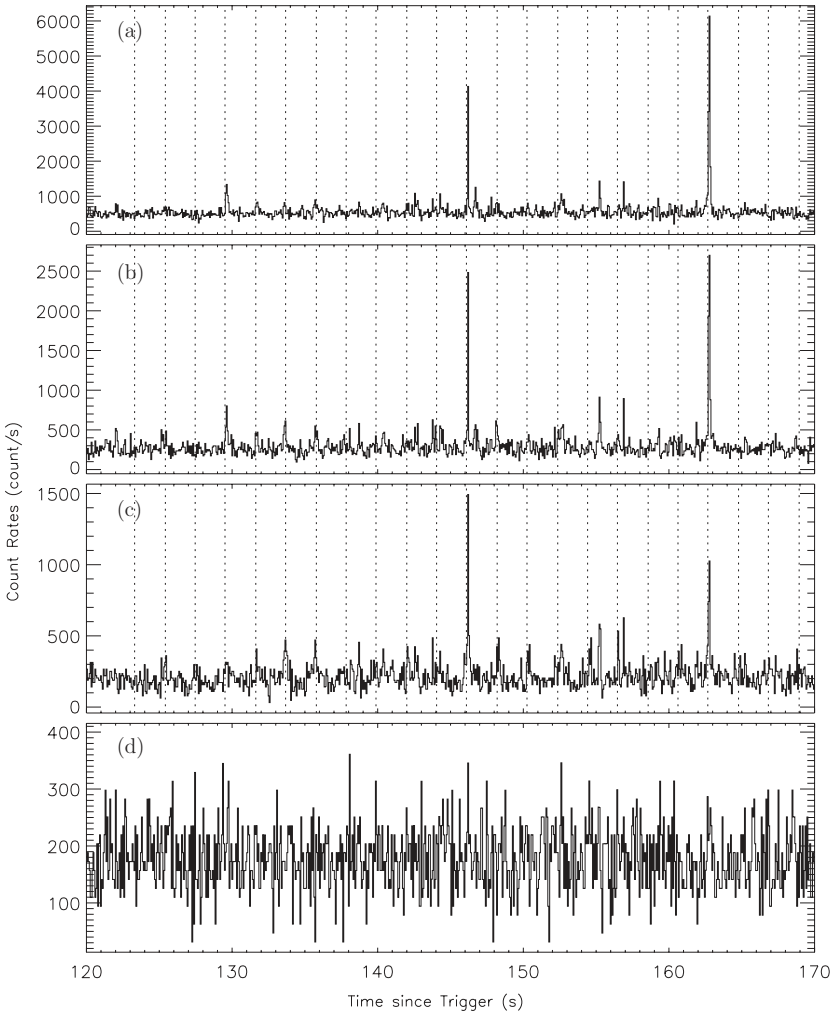

Figure 2. Light curve of SGR J1550–5418 in various energy ranges: (a) 12–27 keV, (b) 27–50 keV, (c) 50–102 keV, and (d) 102–293 keV. The pulsations are most prominent between 50 and 102 keV (panel (c), starting at ∼130 s). The bursts have not been removed here from the data. The dashed lines in panels (a)-(c) indicate the times of the pulse maxima (as calculated using barycentered time).

detector Na I 0 (see panel (c) of Figure 2). This is the first time to our knowledge that pulsations *unrelated* to a giant flare from a magnetar were clearly seen in the persistent emission of an SGR, in energies up to 100 keV. To search for a coherent pulse period, we performed a timing analysis over the entire enhancement interval. We first eliminated the times of all the bursts found via our untriggered burst search and converted the remaining burst-free intervals to the solar system barycenter. For each burst we removed 1 s centered at the burst peak; this elimination resulted in a "loss" of ∼21 s during the interval T_0 +90–220 s. As the majority of the SGR bursts had durations <100 ms, our method removed any effect of the burst contributions in the time series. We then generated a Lomb–Scargle periodogram (Lomb 1975; Scargle 1982) over a range of periods from 0.1 s to 10 s using CTIME Burst data in the 50–102 keV band. We found a very significant signal with a Lomb power of 72.6 (chance occurrence probability, $P_c \simeq 10^{-16}$) at a period of 2.0699 ± 0.0024 s, which is consistent with the spin period of SGR J1550–5418. Further, to confirm our detection, we also employed the $Z^2{}_m$ test (with $m = 2$; Buccheri et al. 1983) on the burst-free and barycentered TTE data. We find a coherent signal (with a $Z^2{}_{m=2}$ power of 266, $P_c \simeq 10^{-23}$) at the same period. Our spin period measurement is consistent with the one found for SGR J1550–5418 using contemporaneous X-ray data (*Swift*/XRT; Kuiper et al. 2009; Israel et al. 2009) and radio data (obtained with Parkes; Burgay et al. 2009). Therefore, we clearly confirm with the detection of these hard X-ray pulsations that the enhanced persistent emission seen in the inset of Figure 1 originates from SGR J1550–5418.

Next, we searched in the enhanced persistent emission for evolution in the intensity of the pulsations using a sliding boxcar technique. We found that the pulsed signal peaks over a 90 s interval, from T_0 +120 to 210 s, which encompasses the peak of the enhancement.

Finally, we searched for any other intervals exhibiting pulsed emission in the burst-free continuous CTIME data of 2009 January 22 and during the four subsequent days, using a sliding boxcar of 120 s with 10 s steps. We did not find any additional statistically significant pulsed emission. For the entire search and for all the timing analysis reported here, we used more precise spin ephemeris obtained by contemporaneous *Swift*/XRT, *Chandra*, *XMM-Newton*, and Suzaku observations (G. L. Israel et al. 2010, in preparation).

3.2. Pulse Profiles

To investigate the evolution of the pulse profiles with energy, we folded the burst-free TTE data spanning 120 s (from

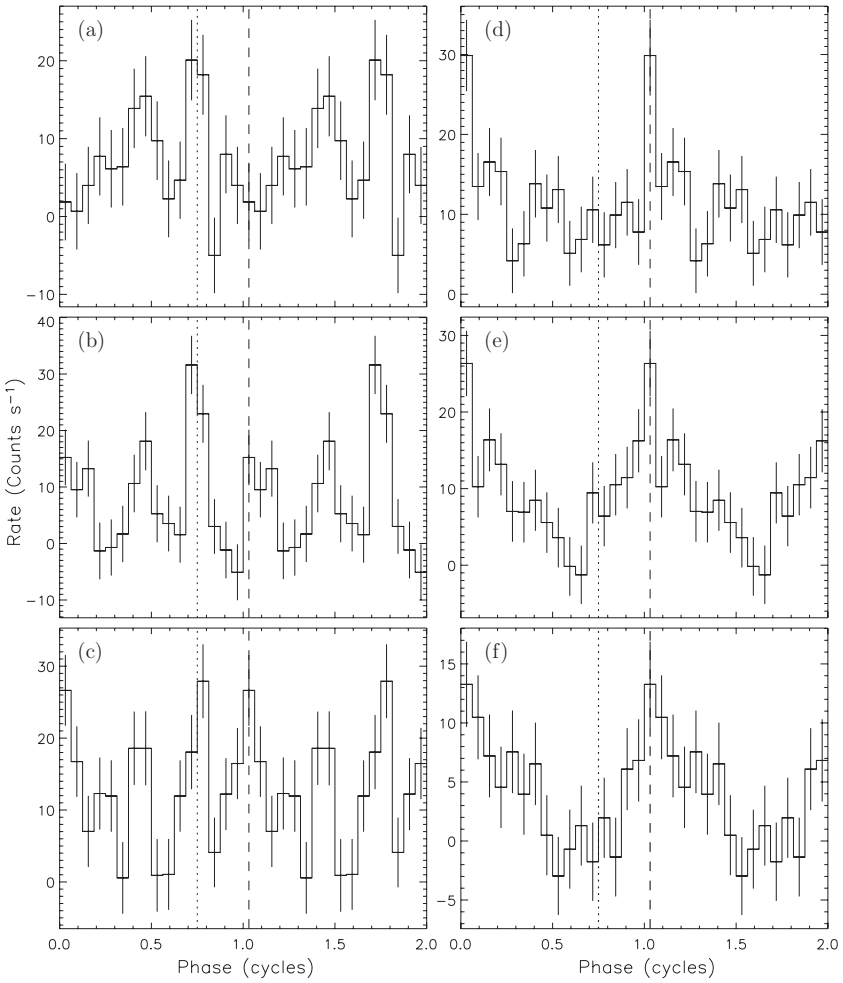

Figure 3. Pulse profiles of SGR J1550–5418 in equal logarithmic energy intervals: (a) 10–14 keV, (b) 14–22 keV, (c) 22–33 keV, (d) 33–50 keV, (e) 50–74 keV, and (f) 74–110 keV. Two cycles are plotted for clarity. The vertical dotted and dashed lines are explained in Section 3.2.

T_0 + 100 s to T_0 + 220 s, which includes the strongest pulsation period as found above) with the spin ephemeris of SGR J1550–5418. We estimated the background level using the data segment between T_0 and T_0 + 60 s. Figure 3 shows the source pulse profiles during the enhanced emission interval in six energy bands that have the same logarithmic width. The pulse profiles above 110 keV are consistent with random fluctuations, and thus not shown.

Figure 3 indicates that the SGR J1550–5418 pulse profiles in the three lowest energy bands are most likely complex (multi-peaked). While the two lowest energy band profiles are dominated by the structure around phase 0.7–0.8 (indicated by the dotted lines in Figure 3), in the 14–22 keV band we see the emergence of another structure around phase 0.0 (indicated by the dashed lines in Figure 3). This pulse becomes equally prominent in the 22–33 keV range and then dominates in the 33–50 keV band. The pulse profile changes remarkably in the 50–74 keV band, which is the most statistically significant of all the energy bands investigated, and is distinguished by a broad structure that peaks at around phase 0.0. The 74–110 keV profile resembles the 50–74 keV one. As noted above, the pulse profile above 110 keV is consistent with random fluctuations. Therefore, our results set an observed upper energy bound of 110 keV for the hard X-ray pulsations in SGR J1550–5418 during this enhanced emission episode.

3.3. Pulsed Fraction

We computed the rms pulsed fraction using a Fourier based approach as described in Woods et al. (2007). In summary, we take the Fourier transform of each pulse profile, then we calculate the rms pulsed flux by taking the Fourier coefficients of up to third harmonic into account, and finally obtain the pulsed fraction values by dividing the rms pulsed flux by the phase-averaged flux. In Figure 4, we show the pulsed fraction spectrum of SGR J1550–5418 in the same energy bands as in Figure 3.

Although marginally significant, there is an indication of a minimum in the rms pulsed fraction around ∼30 keV. The rms reaches its maximum value of 0.55 ± 0.12 in the 50–74 keV band, and then dips below detection at energies greater than ∼110 keV. We will discuss the implications of these results along with the results of our spectral analysis in Section 5.

3.4. Search for High-frequency Quasi-periodic Oscillations

We also searched the period of enhanced emission for any signs of high-frequency quasi-periodic oscillations (QPOs) similar to those seen in the aftermath of SGR giant flares and attributed to the excitation of global seismic modes (Israel et al. 2005; Strohmayer & Watts 2005, 2006; Watts & Strohmayer 2006). Using TTE data from the three detectors (Na I 0, 1,

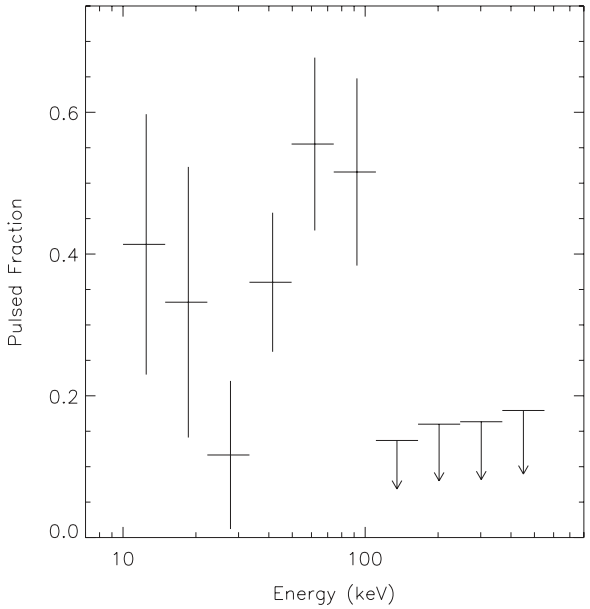

Figure 4. Evolution of rms pulsed fraction of SGR J1550–5418 as a function of energy. Uncertainties are 1σ. The energy bands are the same as those used in Figure 3.

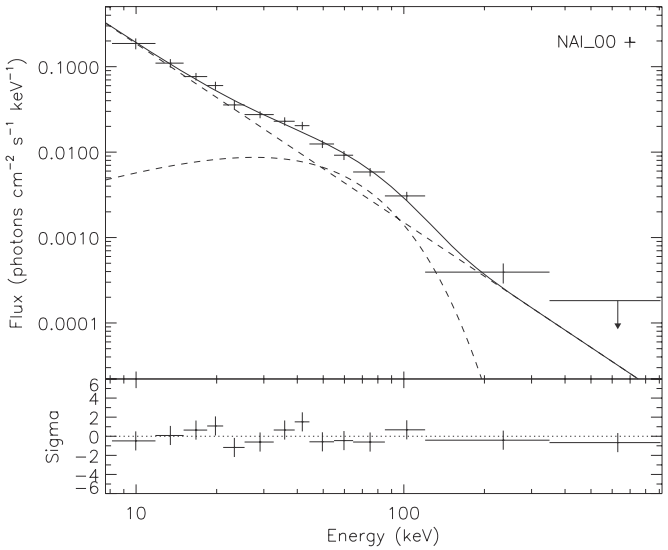

Figure 5. Photon spectrum of the time interval T_0 + 122 to 169 s. The blackbody and power-law components are shown separately with dashed curves. The data are binned for display purpose only. A 3σ upper limit is shown for the highest energy bin.

and 3) with smallest detector zenith angles to the source (and not occulted by the LAT), we selected photons with energies less than 100 keV, where the enhanced emission dominates. We searched the burst-free data set for periodic and quasi-periodic oscillations (1 Hz and 2 Hz resolution) and found no significant signals even on timescales as short as 1 s. During the period when the emission is strongest (T_0 + 100 – 200 s), the 3σ upper limit on the amplitude of QPOs with frequencies in the range 100–4096 Hz is 7.5% rms.

The upper limits are less constraining for frequencies below 100 Hz. A rotational phase-dependent search also revealed no significant signals. Finally, with the bursts included, we searched for short-lived QPOs excited by each event: again, we found nothing significant.

4. SPECTRAL PROPERTIES OF PULSED HARD X-RAYS

4.1. Time-integrated and Time-resolved Spectral Analysis

We analyzed time-integrated and time-resolved spectra of the enhanced emission, using the *RMFIT (3.1rc1)* spectral analysis software developed for the GBM data analysis.[12] Similar to the timing analysis, we excluded all bursts identified with the untriggered search within the enhancement period. Here, we removed up to 3 s of data per burst centered at the burst peak, to account for spectral contributions from the wings of each burst; this elimination resulted in a loss of ∼25 s during the interval T_0 + 70–220 s. We note that although some weak bursts may still be included in our enhanced emission spectra, the very small intensities of these bursts have practically no effect on our spectral analysis results. The spectral study of the untriggered bursts within the enhanced emission indicates that their spectra are different from the enhanced emission spectra (A. J. van der Horst et al. 2010, in preparation). For this analysis, we used only the CSPEC Burst data (8.6–897 keV) of detector Na I 0, which initially had the smallest detector zenith angle to the source (15°) and to which the source was visible through most of the enhanced emission.

Since the Detector Response Matrices (DRMs) of GBM are time dependent due to the continuous slewing of the spacecraft, a DRM should be generated for every 2°–3° of slewing (corresponding to every ∼20–50 s of data). For this analysis, we generated DRMs for every 50 s starting from T_0, using GBMRSP *v1.7* (see Meegan et al. 2009, for a detailed description of the GBM response generation). We used a DRM generated at T_0 + 150 s for the time-integrated spectrum (72–248 s), and three DRMs generated at T_0 + 100, 150, and 200 s, respectively, for the time-resolved spectra: each DRM was centered at the mid-time of the accumulation time span of each spectrum. The background spectrum was determined by fitting a third-order polynomial function to each energy channel using the burst-free intervals (T_0−286 to T_0−43 s, 1008–1196 s, and 1941–2427 s), with a total accumulation time of 896 s.

We found clear evidence for spectral curvature below 100 keV in the time-integrated spectrum of the entire burst-free enhancement period (72–248 s): a single power law thus resulted in a very poor fit. We employed five other spectral models; cut-off power law, power law + blackbody, optically thin thermal bremsstrahlung, and single/double blackbody. We found that the time-integrated spectrum is best described by a power law + blackbody (see Figure 5). All other spectral models did not provide better fits mainly because they failed to fit the lower energy excess $\lesssim$10 keV. The best-fit spectral parameters of a power law with an additional blackbody are shown in Table 1. Adding a blackbody (with $kT = 18 \pm 4$ keV) to a power law resulted in the most significant improvement in Cash statistics (Cash 1979) over a single power law (ΔC-stat = 13.5 for 2 degrees of freedom, corresponding to an improvement of 3.25σ).

The average energy flux over the entire enhancement is $(6.5 \pm 2.4) \times 10^{-8}$ erg cm^{-2} s^{-1} (in 8–150 keV), of which the blackbody component accounts for 19%. As stated earlier, the distance estimate to the source is not well constrained; however, assuming a source distance of ∼5 kpc, we estimate a total isotropic emitted energy of $2.9 \times 10^{40} D_5^2$ erg for the entire persistent emission (8–150 keV) during the enhancement.

[12] R. S. Mallozzi, R. D. Preece, & M. S. Briggs: "RMFIT, A Lightcurve and Spectral Analysis Tool." © 2009 Robert D. Preece, Univ. Alabama in Huntsville.

Table 1
Spectral Parameters of the Enhanced Persistent Emission Period of SGR J1550–5418[a]

Time Since T_0	Power Law (PWRL)[b]		Blackbody (BB)		Energy Flux[c] (10^{-8} erg cm^{-2} s)				Cutoff Power Law[d]	
(s)	A ($\times 10^{-4}$ ph s^{-1} cm^2 keV)	γ	N ($\times 10^{-5}$ ph s^{-1} cm^2 keV)	kT (keV)	ΔC-stat	PWRL	BB	F_{BB}/F_{total}	α	E_{peak} (keV)
72–248	10.53 (1.96)	−2.06 (0.10)	1.23 (0.96)	17.7 (3.8)	13.5	5.30 (2.37)	1.22 (0.28)	0.19 (0.08)	...	...
74–117	5.20 (1.30)	−2.15 (0.17)	No BB	...	...	2.85 (3.30)	...	...	...	...
122–169	15.02 (3.05)	−2.09 (0.11)	4.45 (1.58)	17.4 (1.7)	42.9	7.82 (4.47)	4.08 (0.65)	0.34 (0.14)	−1.30 (0.14)	68 (7)
173–223	9.18 (3.28)	−2.14 (0.19)	3.49 (2.12)	16.4 (2.7)	15.3	5.05 (3.75)	2.59 (0.72)	0.34 (0.19)	−1.33 (0.25)	59 (10)
122–223	13.27 (2.29)	−2.08 (0.10)	3.74 (1.50)	16.5 (1.8)	42.5	6.81 (2.99)	2.84 (0.46)	0.29 (0.10)	−1.41 (0.13)	65 (7)

Notes.
[a] 1σ uncertainties are shown in parentheses. ΔC-stat shows an improvement in Cash statistics by adding a blackbody with 2 degrees of freedom to a power law. Cutoff power-law parameters are shown for the cases where the model also provided adequate fits.
[b] Power-law model: $f(E) = A(E/100\ \mathrm{keV})^{\gamma}$.
[c] Flux is calculated in 8–150 keV.
[d] Cutoff Power-law model: $f(E) = A\ \exp[-E(2+\alpha)/E_{peak}](E/100\ \mathrm{keV})^{\alpha}$.

To investigate the evolution of the blackbody component and of the source's spectral properties, in general, we divided the enhanced emission period into three time intervals of ∼50 s each: 74–117 s, 122–169 s, and 173–223 s after the trigger time. The stopping time of the last spectrum was T_0 + 223 s, because the source was occulted by the LAT for Na I 0 around T_0 + 225 s. We employed the same set of photon models as the time-integrated analysis described above. The first spectrum was best fit by a single power law with no evidence of a blackbody or any curvature. The second and third spectra, on the other hand, were best described by power law + blackbody models. In the second spectrum (the peak of the enhancement), the additional blackbody component was statistically most significant (see Figure 5) and remained significant in the third spectrum as well. The ratio of the blackbody flux to the total flux (8–150 keV) was found to be 34% in both intervals. The indices of the underlying power-law component, and the blackbody temperature also remained constant, at ∼−2.1 and ∼17 keV, respectively (within uncertainties; see also Table 1); while the power-law amplitude tracked the photon flux.

We note that the last two time-resolved spectra were also fitted by a cutoff power-law model with the fit being statistically as good as the power law + blackbody model. The difference between the two models becomes apparent only at energies $\gtrsim$200 keV, where the count rates of our data drop dramatically. For a further comparison, we simulated spectra with the best-fit cutoff power-law model for the second spectrum, folded them through the GBM Na I 0 DRM, and fitted the simulated spectra with a power law + blackbody (and vice versa). We found no indication of significant statistical preference between these two models due to the low count rates at higher energies. The best-fit cutoff power-law parameters for the second and third spectra are also shown in Table 1.

Finally, we also analyzed the spectrum integrated over the second and third time intervals (T_0 + 122 to 223 s), in which the blackbody component was found to be very significant. The blackbody + power-law model parameters for this combined spectrum are listed in Table 1. The results were consistent with the time-resolved analysis of the individual spectra described above, and the statistical significance of the blackbody component was similar to that of the second spectrum (ΔC-stat = 42.5, corresponding to a 6.2σ improvement). A cutoff power-law model also provided an adequate fit for this combined spectrum; the best-fit parameters of the cutoff power law are also listed in Table 1.

4.2. Phase-resolved Spectral Analysis

We performed spin-phase-resolved spectral analysis of the pulsed enhanced emission, as follows: we co-added the burst-free spectrum of each pulse (in T_0 + 122 to 223 s, corresponding to second and third time-resolved spectra) using TTE data and extracted a phase-maximum spectrum (between phases 0.75 and 1.25 in Figure 3) and a phase-minimum spectrum (between phases 0.25 and 0.75). The spin phase for each photon was calculated using barycentered times, as was done for the timing analysis. We calculated the background spectrum, from the burst-free interval at T_0 to T_0 + 60 s.

The spectra of both the phase minimum and maximum were adequately fitted with power-law + blackbody models, where we kept the power-law indices and the blackbody temperatures linked. The values of the linked parameters found in the fit were consistent (within 1σ) with those of the time-integrated spectra (see Table 1; 122–233 s). However, the blackbody component was more significant in the phase-maximum spectrum than in the phase-minimum spectrum. The contributions of the blackbody flux to the total flux were (52 ± 18)% and (35 ± 18)%, in the phase-maximum and phase-minimum spectra, respectively.

5. SUMMARY AND DISCUSSION

We report here the discovery of coherent pulsations in the persistent hard X-ray emission from SGR J1550–5418 in the *Fermi*/GBM data lasting ∼150 s. Coherent pulsations with a 55% rms pulse fraction have never been detected in the persistent emission at these high energies from a magnetar as yet. These pulsations were detected *only* at the onset of a major bursting episode and were not directly related to a major burst or flare from the source. The pulse period is consistent with the spin period of SGR J1550–5418 as measured with contemporaneous *Swift*/XRT observations, thus confirming SGR J1550–5418 as the origin of the enhanced emission. We estimate the total isotropic-equivalent emitted energy during the persistent emission (i.e., excluding burst contributions) to be $2.9 \times 10^{40} D_5^2$ erg. The thermal component accounts for 19% of the total emitted energy; i.e., $5.6 \times 10^{39} D_5^2$ erg is emitted as blackbody.

The fact that this enhanced emission was detected at the onset of a major bursting episode without evidence of direct association to any particular burst or flare immediately before the emission is very intriguing. Intermediate flares with pulsating tails were observed from SGR 1900+14 (Ibrahim et al. 2001; Lenters et al. 2003) and very recently from SGR J1550–5418 (Mereghetti et al. 2009; ∼6 hr after T_0). Thermal components were also found in the decaying tails of intermediate events from SGR 1900+14 with much lower blackbody temperatures of ∼2 keV (Lenters et al. 2003). The thermal component of the enhanced emission we report here is hotter (17 keV), exhibits a strong dependence of the pulse profile with energy with a very high rms pulsed fraction (up to 55%), and is clearly not associated with a decaying event tail. Energetically, however, the fluence of this enhanced emission is comparable to that of tail emission of the intermediate flares from SGR 1900+14.

Our timing analysis showed that the detection of pulsations is most significant in the 120–210 s interval after trigger. We find that the spectrum requires a blackbody component along with a power law between 122 and 223 s, which is consistent with the time interval of the most significant detection of pulsations. Moreover, as determined by the energy dependent pulse profiles and rms pulsed fractions, we find that the high-energy pulsations are most significant in the 50–74 keV range. Strikingly, the blackbody component of the enhanced persistent emission spectrum peaks at around 51 keV (i.e., the Wien peak of 17 keV; see Figure 5). These two independent pieces of evidence lend strong support for a blackbody radiation component to account for the curvature in the spectrum of the enhanced emission.

In our spin-phase-resolved spectral analysis, we find that the blackbody flux to the total emission is $(52 \pm 18)\%$ and $(35 \pm 18)\%$ in the phase-maximum and phase-minimum spectra, respectively. This also suggests that a major contribution to the observed pulsations is from the blackbody component. If we assume a surface hot spot during this pulsating interval, then the best-fit blackbody corresponds to an effective radiating area (as projected on the plane of the sky, far from the star) of $S_\infty = \pi D^2 F/(\sigma T^4) \approx 0.046 D_5^2$ km^2, where $T \approx 2 \times 10^8$ K ($kT \approx 17$ keV) is the observed (gravitationally redshifted) temperature. We have used here the blackbody flux at the peak of the pulsations (i.e., phase maximum; $F \approx 5 \times 10^{-8}$ erg cm^{-2} s^{-1}) where the hot spot is expected to be relatively close to face-on, in order to minimize the effects of projection and gravitational lensing by the neutron star, so that S_∞ would be relatively close to the physical area, S, of the hot spot on the neutron star surface. For a circular hot spot, this corresponds to a radius of $\sim 120 D_5$ m.

The rotational energy of magnetars is insufficient for powering their observed emission, since they all have long rotation periods, and their spin-down luminosity is much lower than their observed luminosity. Owing to their slow rotation, only a very small fraction ($\sim R_{\rm NS}\Omega/c \sim 10^{-5}$–$10^{-4}$) of the magnetic flux threading the neutron star corresponds to open field lines (Beloborodov & Thompson 2007). Since the internal field of magnetars can be significantly stronger and more tangled (or twisted) than the external (largely dipole) field, the transfer of magnetic helicity from the interior to the exterior of the neutron star powers magnetar activity (Beloborodov & Thompson 2007). As the internal field twists the stellar crust, the magnetosphere also becomes twisted, possibly in a complex manner (Thompson et al. 2002).

Beloborodov & Thompson (2007) have shown that the rate of energy dissipation in the twisted magnetosphere is $L_{\rm d} = I\Phi_e \sim 10^{38}\Delta\psi (B/10^{15}\,{\rm G})(a/R_{\rm NS})^2(e\Phi_e/10\,{\rm GeV})$ erg s^{-1}, where I is the net current through the corona, Φ_e is the voltage along the twisted magnetic lines, a is the size of a twisted region on the stellar surface, and $\Delta\psi$ characterizes the strength of the twist. Identifying a with the inferred size of the hot spot ($\sim 120 D_5$ m) would imply $a/R_{\rm NS} \sim 10^{-2}$ which is inconsistent with the observed luminosity of the spot, $L_{\rm d} \sim 10^{38} D_5^2$ erg s^{-1} since $e\Phi_e \lesssim 10$ GeV is expected (limited by pair creation) and $\Delta\psi \lesssim 1$ is required for global stability.

It may be possible for the magnetic twist to grow to a global instability level during a highly active bursting period due to frequent starquakes (i.e., $\Delta\psi \gtrsim 1$; Beloborodov & Thompson 2007). As the magnetosphere untwists, a large amount of energy must be dissipated (Lyutikov 2006). A small "trapped fireball"—plasma of $e^\pm$ pairs and photons confined by a closed magnetic field region—could then potentially account for the inferred hot spot, and in particular its roughly constant temperature and size. Confining a "fireball" of energy at least comparable to that emitted by the observed blackbody component, $E_{\rm iso,BB} \approx 5.6 \times 10^{39} D_5^2$ erg, within a region of radius $a \sim 120 D_5$ m requires $E_B(a) = \frac{1}{6} a^3 B^2 > E_{\rm iso,BB}$ or $B \gtrsim 1.4 \times 10^{14} (a/120 D_5\,{\rm m})^{-3/2} (E_{\rm iso,BB}/5.6 \times 10^{39} D_5^2\,{\rm erg})^{1/2}$ G $\approx 1.4 \times 10^{14} D_5^{-1/2}$ G. This is consistent with the surface dipole field of $B \approx 2.2 \times 10^{14}$ G inferred from the measured $P\dot{P}$ (Camilo et al. 2007). Therefore, a sufficiently small closed magnetic loop anchored by the crust could provide the required confinement.

Although the neutron star surface is relatively cold, hot spots may naturally form on the stellar surface since the energy dissipated in the corona is thermalized as it passes through the denser atmosphere and reaches the stellar crust. The large pulsed fraction implies that the emitting region responsible for the pulsations, which we identify with one or two hot spots on the stellar surface, is mostly or totally obscured during certain rotation phases. This implies that if we are observing emission from two hot spots (of similar temperature) then they cannot be located too far from each other (for example, they cannot be antipodal), as most of the stellar surface is visible to an observer at infinity at any given time because of strong gravitational lensing by the neutron star.

Moreover, we might be observing two hot spots, possibly corresponding to the two footpoints of a twisted magnetic flux tube (or two magnetically confined regions), where the second hot spot is somewhat cooler and dominates the pulsed emission below ∼20 keV. This might explain the energy dependence of the pulse profiles (see Figure 3), with the appearance of a second peak at lower energies (below ∼33 keV, at a phase of ∼0.75), as well as the increase in the rms pulsed fraction at the lowest energies (with a local minimum around ∼28 keV; see Figure 4) and the peak at ∼60 keV corresponding to the hotter hot spot.

This blackbody emission is expected to be accompanied by non-thermal, high-energy radiation produced by collisionless dissipation. Beloborodov & Thompson (2007) estimate that the luminosities in the high-energy and blackbody components should be comparable. This is in good agreement with our observations of SGR J1550–5418, where the high-energy (power law) and blackbody contribution to the total luminosity were found to be 65% and 35%, respectively, for the time-resolved spectra. These contributions were 48% and 52% in the phase-resolved pulse-maximum spectrum.

In conclusion, the area of the blackbody emitting region is the smallest "hot spot" measured for a magnetar, which likely arises from magnetically confined hot plasma on the neutron star

surface, possibly caused by the gradual dissipative untwisting of the magnetosphere (Lyutikov 2006). If the total radiated energy was initially confined to the inferred extremely small size of the enhanced emission region (as in a mini "trapped fireball" scenario), this would indicate a very large magnetic energy density (for $B \gtrsim 1.4 \times 10^{14} D_5^{-1/2}$ G), similar to the "trapped fireball" model for the tails of SGR giant flares. The observed enhanced emission that we report here is much less energetic than a giant flare tail, while its energy is comparable to the tail energy of intermediate events and at the high end of typical SGR bursts. Despite some distinct properties, the enhanced emission of SGR J1550–5418 carries various flavors of all three SGR phenomena, and thus it is most likely related to the very pronounced bursting activity that immediately followed it.

We thank the referee, Dr. F. Camilo, for his valuable comments. This publication is part of the GBM/Magnetar Key Project (NASA grant NNH07ZDA001-GLAST, PI: C. Kouveliotou). We thank G. L. Israel and A. Tiengo for providing the precise spin ephemeris and source distance, respectively, prior to their publication. Y.K. and E.G. acknowledge EU FP6 Transfer of Knowledge Project "Astrophysics of Neutron Stars" (MTKD-CT-2006-042722). J.G. gratefully acknowledges a Royal Society Wolfson Research Merit Award. E. R.-R. thanks the Packard Foundation for support. A.J.v.d.H. was supported by an appointment to the NASA Postdoctoral Program at the MSFC, administered by Oak Ridge Associated Universities through a contract with NASA.

REFERENCES

Beloborodov, A. M., & Thompson, C. 2007, ApJ, 657, 967
Buccheri, R., et al. 1983, A&A, 128, 245
Burgay, M., et al. 2009, Astron. Tel., 1913
Camilo, F., et al. 2006, Nature, 442, 892
Camilo, F., et al. 2007, ApJ, 666, L93
Cash, W. 1979, ApJ, 228, 939
Duncan, R. C., & Thompson, C. 1992, ApJ, 392, L9
Gelfand, J. D., & Gaensler, B. M. 2007, ApJ, 667, 1111
Halpern, J. P., et al. 2005, ApJ, 632, L29
Ibrahim, A. I., et al. 2001, ApJ, 558, 237
Israel, G. L., et al. 2005, ApJ, 628, L53
Israel, G. L., et al. 2009, ATel., 1770
Kouveliotou, C., et al. 1998, Nature, 393, 235
Kouveliotou, C., et al. 2009, GCN Circ. #8915
Kuiper, L., den Hartog, P. R., & Hermsen, W. 2009, ATel., 1921
Lenters, G. T., et al. 2003, ApJ, 587, 761
Lomb, N. R. 1975, Ap&SS, 39, 447
Lyutikov, M. 2006, MNRAS, 367, 1594
Meegan, C., et al. 2009, ApJ, 702, 791
Mereghetti, S. 2008, A&AR, 15, 225
Mereghetti, S., et al. 2009, ApJ, 696, L74
Scargle, J. D. 1982, ApJ, 263, 835
Strohmayer, T. E., & Watts, A. L. 2005, ApJ, 632, L111
Strohmayer, T. E., & Watts, A. L. 2006, ApJ, 653, 593
Sugizaki, M., et al. 2001, ApJS, 134, 77
Thompson, C., Lyutikov, M., & Kulkarni, S. R. 2002, ApJ, 574, 332
Tiengo, A., et al. 2010, ApJ, submitted (arXiv:0911.3064v2)
Watts, A. L., & Strohmayer, T. E. 2006, ApJ, 637, L117
Woods, P. M., & Thompson, C. 2006, in Cambridge Astrophys. Ser. 39, Compact Stellar X-ray Sources, ed. W. H. G. Lewin & M. van der Klis (Cambridge: Cambridge University Press), 547
Woods, P. M., et al. 2007, ApJ, 654, 470